

國立臺灣大學理學院物理學研究所



碩士論文

Department of Physics

College of Science

National Taiwan University

Master Thesis

在 GAMER 中實現宇宙射線

The Implementation of Cosmic Rays in GAMER

陳俊延

Chun-Yen Chen

指導教授: 薛熙于 博士

Advisor: Hsi-Yu Schive, Ph.D.

中華民國 112 年 7 月

July, 2023





Acknowledgements

感謝薛熙于老師，老師總是給我具有建設性的意見以及心靈上的支持。感謝我的家人可以讓我在沒有經濟壓力的情況下念完碩士。感謝來自於國家理論科學研究中心 (NSTC) 以及 MoE 的贊助，讓我們可以進行此項研究。感謝闕志鴻老師以及胡德邦老師總是在開會的時候給出精闢的觀點以及意見。感謝蘇冠銘學長、黃新豪學長、Alex 還有實驗室的大家總是在我需要的時候給我技術性的幫助。感謝亮宇以及霽佑在修課的時候總是給我許多幫助，如果沒有你們的話我應該研究所的課都過不了。感謝過去所有被我帶過普物的學生，你們總是會給我一些全新的觀點，以及我從來沒想過的想法。感謝江府峻教授以及楊湘怡教授在我對於未來感到迷茫的時候給我對於職涯非常實用的觀點。感謝 OpenAI 的 Chat-GPT 幫我解決這篇論文上的錯字、文法以及修飾文字。最後我想感謝製作這個論文模板的大大，讓我省下許多研究排版的時間。





摘要

我們擴展了 GAMER-2 的功能，以支持宇宙射線之物理，其中包括單一能量通道、平流、非等向性擴散以及與熱氣體的動態耦合。我們將寫好的程式用下面的測試問題：聲波、震波管以及數個非等向性擴散測試來檢驗程式的準確性。這些測試的結果都有二階精確。除此之外，我們也讓宇宙射線的計算支援 GAMER-2 的進階功能，其中包括自適應網格、混合的 OpenMP/MPI 平行以及圖形顯示卡 (GPU) 的平行加速。在未來，我們預計再未來增加更多宇宙射線的物理像是多能量通道、宇宙射線流以及宇宙射線熱效應。

關鍵字： GAMER2、宇宙射線、FLASH、GPU 加速





Abstract

We extend GAMER-2 to support cosmic rays with a single energy channel, advection, anisotropic diffusion, and dynamical coupling to thermal gas. To verify the accuracy, we conduct a series of numerical experiments, including acoustic wave, shock-tube problem, and several anisotropic diffusion tests. All tests achieve second-order accuracy. Furthermore, our extension inherits the advanced features of GAMER-2, including adaptive mesh refinement, hybrid OpenMP/MPI parallelization, and graphics processing unit (GPU) acceleration. We are planning to implement multiple energy channels, cosmic rays streaming, and heating.

Keywords: GAMER2, Cosmic Rays, FLASH, GPU boost





Contents

	Page
Verification Letter from the Oral Examination Committee	i
Acknowledgements	iii
摘要	v
Abstract	vii
Contents	ix
List of Figures	xi
List of Tables	xv
Chapter 1 Introduction	1
Chapter 2 Governing equations	3
2.1 MHD with CRs	3
2.2 Numerical method	5
2.2.1 MHM-RP with CRs	5
2.2.2 AMR of CRs	9
Chapter 3 Results	11
3.1 Sound Wave	12
3.1.1 With and without background velocity	13
3.1.2 Half Step Update	16

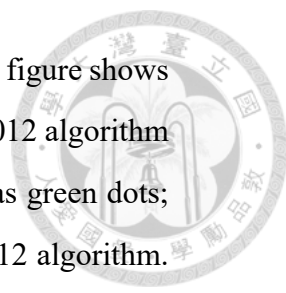
3.2	Shock Tube (without diffusion)	17
3.3	Diffusion	17
3.3.1	Isotropic diffusion	19
3.3.2	Anisotropic diffusion - Gaussian	19
3.3.3	Anisotropic diffusion - Ring	22
3.3.4	Anisotropic diffusion - Blast Wave	23
3.4	AMR	25
3.4.1	Blast wave	25
3.4.2	Shocktube	25
3.5	Performance	26
Chapter 4 Conclusions		29
References		31
Appendix A — GAMER Limiter		37
Appendix B — Analytical Solution of CR Diffusion Equation		43
B.1	1-D solution	43
B.2	3-D solution	44





List of Figures

3.1	Sound wave test of thermal gas and cosmic rays after traveling one wave period with $v_0 = 0$ with resolution $N = 128$. The left panel displays the disturbance in cosmic ray pressure, while the right panel exhibits the perturbation in density along the diagonal direction. Simulation data is plotted with the blue dot symbol; solid red lines represent the analytical solution.	13
3.2	Sound wave test without a background velocity of the cosmic rays and the thermal gas. The figure shows the L1 error convergence. The L1 error of the Yang et al., 2012 algorithm is plotted as blue dots; the L1 error of GAMER is plotted as green dots; the solid blue line is the linear fitting of the Yang et al., 2012 algorithm. L1 error; the solid green line is the linear fitting of GAMER L1 error.	14
3.3	Test the cosmic rays and thermal gas by observing the linear sound wave after it has traveled one wavelength with an initial velocity of $v_0 = 1$, using a resolution of $N = 128$. The figure on the left shows the perturbation of the cosmic rays pressure, and the figure on the right shows the perturbation of density in the diagonal direction. Simulation data is plotted with the blue dot symbol; the solid red lines represent the analytical solution. . . .	15



3.4 Sound wave test of the cosmic rays and the thermal gas. The figure shows the L1 error convergence. The L1 error of the Yang et al., 2012 algorithm is plotted as blue dots; the L1 error of GAMER is plotted as green dots; the solid blue line is the linear fitting of the Yang et al., 2012 algorithm. L1 error; the green solid line represents the linear fit of the GAMER L1 error. 15

3.5 Sound wave test of the cosmic rays and thermal gas. The figure shows the L1 error convergence. The L1 error of GAMER without a half-step update is plotted as blue dots; the L1 error of GAMER with a half-step update is plotted as green dots; the solid blue line is the linear fitting of GAMER without a half-step update L1 error; the solid green line is the linear fitting GAMER with half-step update L1 error. 16

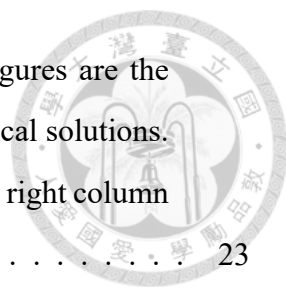
3.6 Shock tube test of the cosmic rays and the thermal gas. The top-left panel of the figure illustrates the density, the top-right panel displays the velocity, the bottom-left panel showcases the internal energy density of the gas, and the bottom-right panel exhibits the energy density of cosmic rays. The green dots show the GAMER simulation data; the orange dots show the Yang et al., 2012 algorithm simulation data; the blue solid lines represent the analytical solution. 18

3.7 The figure shows the Gaussian distribution of cosmic rays energy density time evolution. The analytical solutions are marked as cyan dashed lines. The cosmic rays energy density is marked as blue and orange points at $t = 0$ and $t = 0.5$ respectively. 20

3.8 The L1 error of the isotropic diffusion test. The number of cells is set from 64^3 to 512^2 20

3.9 The x-y slice of the anisotropic diffusion test of the Gaussian distribution cosmic rays. The magnetic field is in the diagonal direction. The left panel is at $t=0$. The right panel is at $t=0.5$ 21

3.10 The L1 error of the two-dimensional anisotropic diffused cosmic rays. . . 21



3.11 The ring test of the anisotropic diffusion. The top row figures are the simulation result, and the bottom row figures are the analytical solutions. The left column is $t = 0$. The middle column is $t = 0.1$. The right column is $t = 200$ 23

3.12 The figure shows the L1 error of the anisotropic diffuse cosmic rays ring test. 24

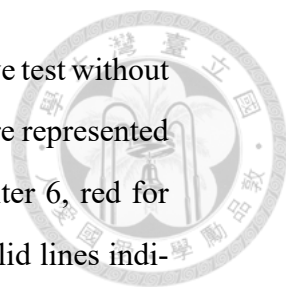
3.13 A x-z slice of the blast wave test of the anisotropic diffusion. The left panel presents the gas density, and the right panel illustrates the energy density of cosmic rays. 25

3.14 A x-z slice of blast wave test with anisotropic diffusion and AMR level up to 3. The left panel presents the gas density, and the right panel illustrates the energy density of cosmic rays. 26

3.15 Shock tube test of cosmic rays and the thermal gas with and without AMR. The top-left panel of the figure illustrates the density, the top-right panel displays the velocity, the bottom-left panel showcases the internal energy density of the gas, and the bottom-right panel exhibits the energy density of cosmic rays. The green squares show the data with AMR; the orange dots represent the data without AMR; the blue solid lines represent the analytical solution of the shock tube. 27

A.1 The L1 error of the one-dimensional linear wave sound wave test without background velocity is shown in the figure. The L1 errors are represented by colored dots: blue for FLASH, green for GAMER limiter 6, red for GAMER limiter 4, and cyan for GAMER limiter 2. The solid lines indicate linear fittings for each L1 error. 38

A.2 The L1 error of the one-dimensional linear wave sound wave test with background velocity is shown in the figure. The L1 errors are represented by colored dots: blue for FLASH, green for GAMER limiter 6, red for GAMER limiter 4, and cyan for GAMER limiter 2. The solid lines indicate linear fittings for each L1 error. 39



A.3 The L1 error of the three-dimensional linear wave sound wave test without background velocity is shown in the figure. The L1 errors are represented by colored dots: blue for FLASH, green for GAMER limiter 6, red for GAMER limiter 4, and cyan for GAMER limiter 2. The solid lines indicate linear fittings for each L1 error. 40

A.4 The L1 error of the three-dimensional linear wave sound wave test with background velocity is shown in the figure. The L1 errors are represented by colored dots: blue for FLASH, green for GAMER limiter 6, red for GAMER limiter 4, and cyan for GAMER limiter 2. The solid lines indicate linear fittings for each L1 error. 41



List of Tables

3.1	The initial condition of the shock tube test. From the top to the bottom, the parameters are density, velocity, gas pressure, and cosmic rays pressure.	17
3.2	The computation time of one time-step with double precision.	26





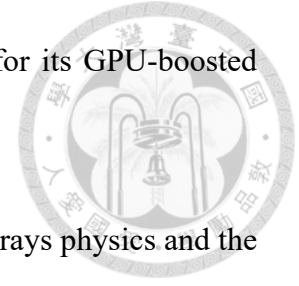
Chapter 1 Introduction

Cosmic rays (CRs) are high-energy particles that originate from outer space and travel through the universe at incredibly high speeds. Cosmic rays can be one of the important physics of the formation of the Fermi bubble [39], and also a heating source of the interstellar medium [32] [15]. Radio Relics are one of the evidence of cosmic rays in galaxy clusters. In recent studies, we found some arc-like, concave Radio Relics called "Wrong Way" Radio Relics near the galaxy clusters [5] [16]. To answer the mechanism of how it forms, we need to add the cosmic rays physics in the code. Cosmic rays could take an important role in star formation [27] [38]. With the cosmic rays feedback, the star formation rate could be slower [2] [28] [7] [22] [11] [18], and launch more powerful winds in the galaxy [29] [3] [17] [19] [13].

To simulate cosmic rays, we need to solve and evolve the distribution of cosmic rays which is dependent on the position, momentum, and time. Such a simulation could be very time-consuming, so we need a more powerful calculation technique to simulate cosmic rays.

Utilizing GPU acceleration is a widely adopted approach to significantly enhance the performance of simulations. For instance, ENZO [6], RAMSES [37], Castro [1], and GAMER (GPU-accelerated Adaptive MESH Refinement) [33] [34].

In this thesis, we choose GAMER, a simulation tool known for its GPU-boosted capabilities, to implement cosmic rays modeling.



In section 2, we will talk about the MHD equation with cosmic rays physics and the numerical method of evolving the cosmic rays. In section 3, we will test our implementation of cosmic rays and compare with Yang et al., 2012 algorithm with a series of tests. In section 4, we will make our conclusions here. Furthermore, in the appendix, we also test how the slope limiter affects the error convergence rate, and provide the analytical solutions of the Gaussian distribution of the cosmic rays diffusion.



Chapter 2 Governing equations

In this section, we will discuss the governing equations of magnetohydrodynamics (MHD) with cosmic rays, the implementation of cosmic rays in GAMER, and the numerical method for solving cosmic rays equations.

2.1 MHD with CRs

Cosmic rays are charged particles whose traveling speed is close to light speed, but the collective speed of cosmic rays is much slower in the galaxy because of scattering by a short coherent length magnetic field. We assume the scattering is strong which means the cosmic rays are trapped by the magnetic field, so the collective speed of cosmic rays is the same as the thermal gas. Also, we assume the cosmic rays to be one species only and share one single energy channel. Meanwhile, we neglect the cosmic rays streaming and heating effect in this thesis.

Based on the assumptions above, we treat cosmic rays as a passive scalar which is a second fluid that has different energy density (or pressure). Hence, we extend the original MHD equations with cosmic rays physics, including cosmic rays diffusion, advection, and dynamical coupling between the cosmic rays and the thermal gas can be written as:



$$\frac{\partial \rho}{\partial t} + \nabla \cdot (\rho \mathbf{v}) = 0 \quad (2.1)$$

$$\frac{\partial \rho \mathbf{v}}{\partial t} + \nabla \cdot \left(\rho \mathbf{v} \mathbf{v} - \frac{\mathbf{B} \mathbf{B}}{4\pi} \right) + \nabla p_{tot} = \rho \mathbf{g} \quad (2.2)$$

$$\frac{\partial \mathbf{B}}{\partial t} - \nabla \times (\mathbf{v} \times \mathbf{B}) = 0 \quad (2.3)$$

$$\frac{\partial e}{\partial t} + \nabla \cdot \left[(e + p_{tot}) \mathbf{v} - \frac{\mathbf{B}(\mathbf{B} \cdot \mathbf{v})}{4\pi} \right] = \rho \mathbf{v} \cdot \mathbf{g} + \nabla \cdot (\boldsymbol{\kappa} \cdot \nabla e_{cr}) \quad (2.4)$$

$$\frac{\partial e_{cr}}{\partial t} + \nabla \cdot (e_{cr} \mathbf{v}) = -p_{cr} \nabla \cdot \mathbf{v} + \nabla \cdot (\boldsymbol{\kappa} \cdot \nabla e_{cr}) \quad (2.5)$$

where ρ is the thermal gas density, p_{tot} is the total pressure which can be expressed as (2.6), \mathbf{v} is the velocity, \mathbf{g} is the gravitational field, \mathbf{B} is the magnetic field, $\boldsymbol{\kappa}$ is the diffusion tensor, e_{cr} is the cosmic rays energy density, p_{cr} is pressure of cosmic rays, and e is the total energy density which can be express as (2.7) where e_{th} is the energy density of the thermal gas, and the $\gamma = 5/3$ is the adiabatic index of the thermal gas [23] [4].

$$p_{tot} = (\gamma - 1)e_{th} + (\gamma_{cr} - 1)e_{cr} + B^2/8\pi \quad (2.6)$$

$$e = 0.5\rho v^2 + e_{th} + e_{cr} + B^2/8\pi \quad (2.7)$$

The equation of state of cosmic rays

$$p_{cr} = e_{cr} (\gamma_{cr} - 1) \quad (2.8)$$

where $\gamma_{cr} = 4/3$ is the effective adiabatic index of cosmic rays [21].



2.2 Numerical method

In GAMER, there are two fluid schemes supporting MHD physics which are the MUSCL-Hancock method with Riemann prediction (MHM-RP) [12] [41] and corner transport upwind method (CTU) [8] [40]. Since the adiabatic work term and the diffusion term is trivial to implement in MHM-RP, we choose MHM-RP as the cosmic rays update scheme in this thesis. MHM-RP is a variant of the MUSCL-Hancock method solver. The main difference is that MHM-RP calculates the half-step flux by the Riemann solver, so it is more time-consuming.

2.2.1 MHM-RP with CRs

The algorithm of MHM-RP with cosmic rays can be summarized as the following pseudo-code. We add two more steps, step 5, and 7 to achieve the evolution of cosmic rays.

Algorithm 1 Single time step of MHM-RP

- 1: Calculate_HalfStepFlux()
 - 2: Calculate_HalfStepElectricField()
 - 3: Update_HalfMagneticField()
 - 4: Update_HalfFluid()
 - 5: **Update_HalfCR()**
 - 6: DataReconstruction()
 - 7: Calculate_FullStepFlux()
 - 8: Update_FullMagneticField()
 - 9: Update_FullFluid()
 - 10: **Update_FullCR()**
-

There are two cosmic rays terms that need to be implemented in GAMER, one is the adiabatic work, and the other one is the diffusion term. In addition, we also have a Courant–Friedrichs–Lewy (CFL) condition [10] for the cosmic rays. The adiabatic work

term of the cosmic rays $-p_{cr} \nabla \cdot \mathbf{v}$ can be implemented as (2.9) and (2.10) which are the half step and the full step respectively.



$$-p_{cr,i,j,k}^n \cdot \left[\frac{F_{i+1/2,j,k}^n - F_{i-1/2,j,k}^n}{\Delta x} + \frac{F_{i,j+1/2,k}^n - F_{i,j-1/2,k}^n}{\Delta y} + \frac{F_{i,j,k+1/2}^n - F_{i,j,k-1/2}^n}{\Delta z} \right] \quad (2.9)$$

$$-p_{cr,i,j,k}^{n+1/2} \cdot \left[\frac{F_{i+1/2,j,k}^{n+1/2} - F_{i-1/2,j,k}^{n+1/2}}{\Delta x} + \frac{F_{i,j+1/2,k}^{n+1/2} - F_{i,j-1/2,k}^{n+1/2}}{\Delta y} + \frac{F_{i,j,k+1/2}^{n+1/2} - F_{i,j,k-1/2}^{n+1/2}}{\Delta z} \right] \quad (2.10)$$

The $F_{i-1/2,j,k}^n$ and $F_{i+1/2,j,k}^n$ are the fluxes which can be defined as [24]

$$F_{i-1/2,j,k}^n = \begin{cases} \frac{F_{i-1/2,j,k}^{n,\rho}}{\rho_{i-1,j,k}} & , \text{ if } F_{i-1/2,j,k}^{n,\rho} > 0 \\ \frac{F_{i-1/2,j,k}^{n,\rho}}{\rho_{i,j,k}} & , \text{ if } F_{i-1/2,j,k}^{n,\rho} \leq 0 \end{cases} \quad (2.11)$$

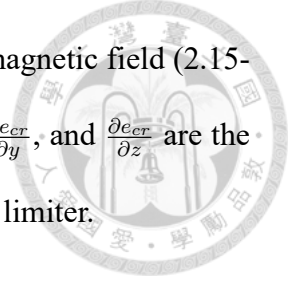
$$F_{i+1/2,j,k}^n = \begin{cases} \frac{F_{i+1/2,j,k}^{n,\rho}}{\rho_{i,j,k}} & , \text{ if } F_{i+1/2,j,k}^{n,\rho} > 0 \\ \frac{F_{i+1/2,j,k}^{n,\rho}}{\rho_{i+1,j,k}} & , \text{ if } F_{i+1/2,j,k}^{n,\rho} \leq 0 \end{cases} \quad (2.12)$$

where the $F_{i+1/2,j,k}^{n,\rho}$ is the density flux between the cell (i, j, k) and $(i + 1, j, k)$, and n is the n -th time step of the simulations.

In the algorithm from Yang et al., 2012, this term will only be updated in the full step, and the pressure of cosmic rays in this term is $(p_{cr,i,j,k}^n + p_{cr,i,j,k}^{n+1})/2$, so they reach around 1.5-th order of accuracy. We added the half-step update in GAMER to approach the second-order accuracy. We will discuss it more in the section 3.1.

The diffusion term of the cosmic rays $\nabla \cdot (\kappa \cdot \nabla e_{cr})$ can be implemented as (2.13)

where b_x is the unit magnetic field (2.14), \bar{b}_y and \bar{b}_z are the average magnetic field (2.15-2.16), $\bar{\kappa}_{\parallel}$ and $\bar{\kappa}_{\perp}$ are the average diffusion coefficient (2.17), $\frac{\partial e_{cr}}{\partial x}$, $\frac{\partial e_{cr}}{\partial y}$, and $\frac{\partial e_{cr}}{\partial z}$ are the slope of the cosmic rays, and L operator can be any kind of the slope limiter.



$$F_{i+1/2,j,k}^n = - (\bar{\kappa}_{\parallel} - \bar{\kappa}_{\perp}) b_x \left[b_x \frac{\partial e_{cr}}{\partial x} + \bar{b}_y \frac{\partial e_{cr}}{\partial y} + \bar{b}_z \frac{\partial e_{cr}}{\partial z} \right] - \bar{\kappa}_{\perp} \frac{\partial e_{cr}}{\partial x} \quad (2.13)$$

$$b_x = b_{x,i+1/2,j,k}^n \quad (2.14)$$

$$\bar{b}_y = (b_{y,i,j-1/2,k}^n + b_{y,i+1,j-1/2,k}^n + b_{y,i,j+1/2,k}^n + b_{y,i+1,j+1/2,k}^n)/4 \quad (2.15)$$

$$\bar{b}_z = (b_{z,i,j,k-1/2}^n + b_{z,i+1,j,k-1/2}^n + b_{z,i,j,k+1/2}^n + b_{z,i+1,j,k+1/2}^n)/4 \quad (2.16)$$

$$\frac{2}{\bar{\kappa}_{\parallel}} = \frac{1}{\kappa_{\parallel,i,j,k}} + \frac{1}{\kappa_{\parallel,i+1,j,k}}, \quad \frac{2}{\bar{\kappa}_{\perp}} = \frac{1}{\kappa_{\perp,i,j,k}} + \frac{1}{\kappa_{\perp,i+1,j,k}} \quad (2.17)$$

$$\frac{\partial e_{cr}}{\partial x} = \frac{e_{cr,i+1,j,k} - e_{cr,i,j,k}}{\Delta x} \quad (2.18)$$

$$\frac{\partial e_{cr}}{\partial y} = L \left[L \left(\frac{\partial e_{cr}}{\partial y} \Big|_{i,j-1/2,k}, \frac{\partial e_{cr}}{\partial y} \Big|_{i,j-1/2,k} \right), L \left(\frac{\partial e_{cr}}{\partial y} \Big|_{i+1,j+1/2,k}, \frac{\partial e_{cr}}{\partial y} \Big|_{i+1,j+1/2,k} \right) \right] \quad (2.19)$$



$$\overline{\frac{\partial e_{cr}}{\partial z}} = L \left[L \left(\frac{\partial e_{cr}}{\partial z} \Big|_{i,j,k-1/2}, \frac{\partial e_{cr}}{\partial z} \Big|_{i,j,k+1/2} \right), L \left(\frac{\partial e_{cr}}{\partial z} \Big|_{i+1,j,k-1/2}, \frac{\partial e_{cr}}{\partial z} \Big|_{i+1,j,k+1/2} \right) \right] \quad (2.20)$$

Here we choose L to be Monotonized Central (MC) limiter which can be expressed as (2.21).

$$L(a, b) = \text{minmod} \left[2\text{minmod}(a, b), \frac{a+b}{2} \right] \quad (2.21)$$

$$\text{minmod}(a, b) = \begin{cases} \min(a, b) & , \text{ if } a, b > 0 \\ \max(a, b) & , \text{ if } a, b < 0 \\ 0 & , \text{ if } ab \leq 0 \end{cases} \quad (2.22)$$

Finally, the CFL condition of cosmic rays will be limited by the diffusion coefficient.

$$\Delta t \leq \frac{\min [\Delta x^2, \Delta y^2, \Delta z^2]}{2 (\kappa_{\parallel} + \kappa_{\perp})} \quad (2.23)$$

The cosmic rays will be updated as

$$e_{cr,i,j,k}^{n+1} = e_{cr,i,j,k}^n - \Delta t \left[\frac{F_{i+1/2,j,k}^n - F_{i-1/2,j,k}^n}{\Delta x} + \frac{F_{i,j+1/2,k}^n - F_{i,j-1/2,k}^n}{\Delta y} + \frac{F_{i,j,k+1/2}^n - F_{i,j,k-1/2}^n}{\Delta z} \right] \quad (2.24)$$

2.2.2 AMR of CRs



Adaptive Mesh Refinement (AMR) is one of the essential tools of astrophysics code now. We can save a lot of computational resources, increase the simulation resolution on the fine structures or shocks that we interest in, and also enhance the accuracy at the same time. There are several ways to identify whether the region needs to be refined or not, for instance, the gradient of the density, the value of the thermal gas speed, and the error estimator.

Here we adopted two types of AMR refinement criteria for cosmic rays, one is dependent on the value of cosmic rays energy density, and the other one is dependent on the Löhner error estimator [25] of cosmic rays energy density.





Chapter 3 Results

In this section, we will test the implementation of cosmic rays separately. For the adiabatic work term, we tested it by the acoustic wave and the shock-tube tests. For the diffusion term, we tested with the Gaussian distribution diffusion and the ring diffusion. Finally, we also tested the combination of adiabatic work, diffusion, and AMR by the blast wave and shock-tube test.

In the following section, we use HLLD [26] as Riemann solver, and piecewise-parabolic method (PPM) [9] as the data-reconstruction method. Let us first define some terms we often used in this section. N stands for the number of cells in the simulation box. The L1 error of cosmic rays energy density is defined as

$$L1(e_{cr}) = \frac{1}{N} \sum_i \left| 1 - \frac{e_{cr,i}}{e_{cr}(\mathbf{r}_i)} \right| \quad (3.1)$$

where the $e_{cr}(\mathbf{r}_i)$ is the analytical solution and $e_{cr,i}$ is the numerical solution of i^{th} cell accordingly.

Since Yang et al., 2012 implement the cosmic rays algorithm in FLASH [14], another astrophysics code, we use the label FLASH to represent the simulation data run by Yang et al., 2012 algorithm in the figure of this section.



3.1 Sound Wave

In this test problem, a sound wave propagates along the diagonal direction composed by the cosmic rays, and the thermal gas is set in the square simulation box with size $L = 1$ [31].

This test problem considers the coupling between the two fluids, the cosmic rays, and the thermal gas. Furthermore, we will show how the half-step update of the adiabatic term effect the error convergence rate. The perturbations of the fluid satisfy the following relations

$$\frac{\delta\rho}{\rho_0} = \frac{\delta p}{\gamma p_0} = \frac{\delta p_{cr}}{\gamma_{cr} p_{cr,0}} = \frac{\delta v}{c_s} \quad (3.2)$$

where $\delta\rho$, δv , δp , and δp_{cr} are perturbations of density, velocity, gas pressure, and pressure of cosmic rays respectively, ρ_0 , p_0 , and $p_{cr,0}$ are background value of density, gas pressure, and cosmic rays pressure respectively. The sound speed c_s is given by

$$c_s = \sqrt{\frac{\gamma p_0 + \gamma_{cr} p_{cr,0}}{\rho_0}} \quad (3.3)$$

In the following tests, we set a sinusoidal wave moving in the diagonal direction with wavelength $1/\sqrt{3}$ which means there will be three complete waves in the diagonal direction, and other initial conditions of the fluid variables are $\rho_0 = 1.0$, $p_0 = 1.0$, $p_{cr} = 1.0$, and $\delta v = 10^{-6}$. The background velocity of the simulations is set differently, we will discuss it in the later subsections. The wave travels periodically in the simulation box for one period. For the L1 error, we increase N from 32 to 512 in each direction and estimate



the L1 error of each case.

3.1.1 With and without background velocity

First, we set the background velocity $v_0 = 0$. Figure 3.1 shows the diagonal profile of sound wave travels after one period with a resolution of 128 in each direction.

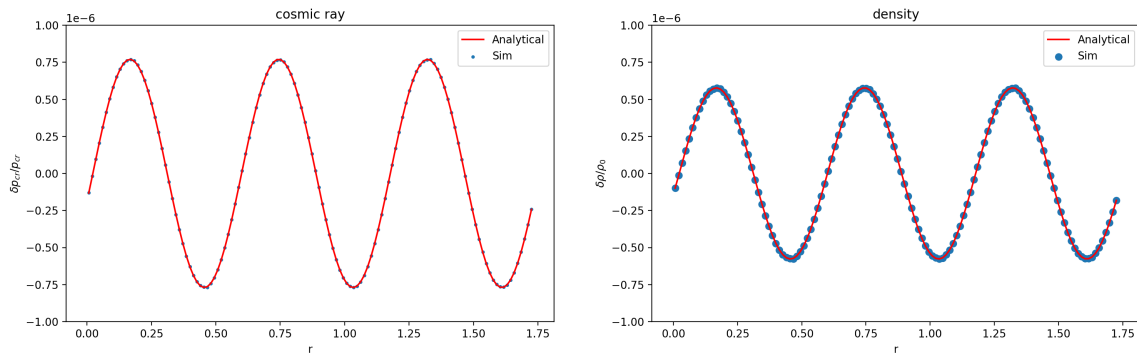


Figure 3.1: Sound wave test of thermal gas and cosmic rays after traveling one wave period with $v_0 = 0$ with resolution $N = 128$. The left panel displays the disturbance in cosmic ray pressure, while the right panel exhibits the perturbation in density along the diagonal direction. Simulation data is plotted with the blue dot symbol; solid red lines represent the analytical solution.

Figure 3.2 shows the L1 error compared with Yang et al., 2012 algorithm with the same setup. The L1 error of Yang et al., 2012 algorithm is proportional to $N^{-1.32}$, and the L1 error of GAMER is proportional to $N^{-1.73}$. Our results show GAMER has a better convergence rate.

Now, we set the background velocity $v_0 = 1$. Figure 3.3 shows the diagonal profile of sound wave travels after one period with resolution $N = 128$ in each direction.

Figure 3.4 shows L1 error compared with Yang et al., 2012 algorithm with the same setup. The L1 error of Yang et al., 2012 algorithm is proportional to $N^{-1.30}$, and the L1 error of GAMER is proportional to $N^{-1.82}$. Again, our results show GAMER has a better convergence rate.

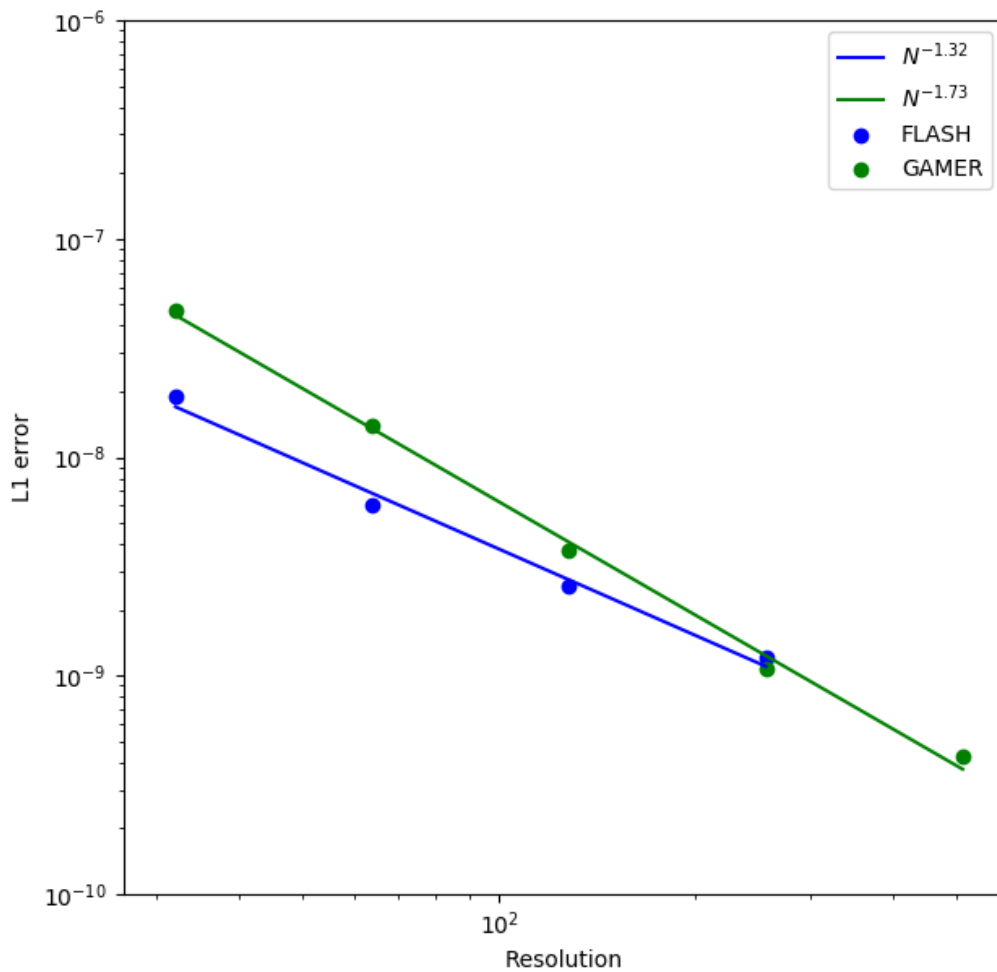


Figure 3.2: Sound wave test without a background velocity of the cosmic rays and the thermal gas. The figure shows the L1 error convergence. The L1 error of the Yang et al., 2012 algorithm is plotted as blue dots; the L1 error of GAMER is plotted as green dots; the solid blue line is the linear fitting of the Yang et al., 2012 algorithm. L1 error; the solid green line is the linear fitting of GAMER L1 error.

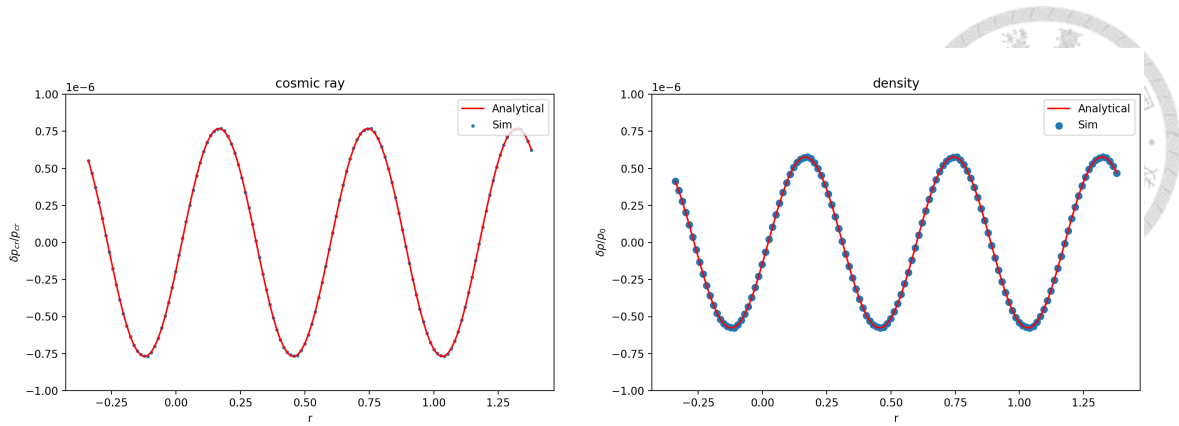


Figure 3.3: Test the cosmic rays and thermal gas by observing the linear sound wave after it has traveled one wavelength with an initial velocity of $v_0 = 1$, using a resolution of $N = 128$. The figure on the left shows the perturbation of the cosmic rays pressure, and the figure on the right shows the perturbation of density in the diagonal direction. Simulation data is plotted with the blue dot symbol; the solid red lines represent the analytical solution.

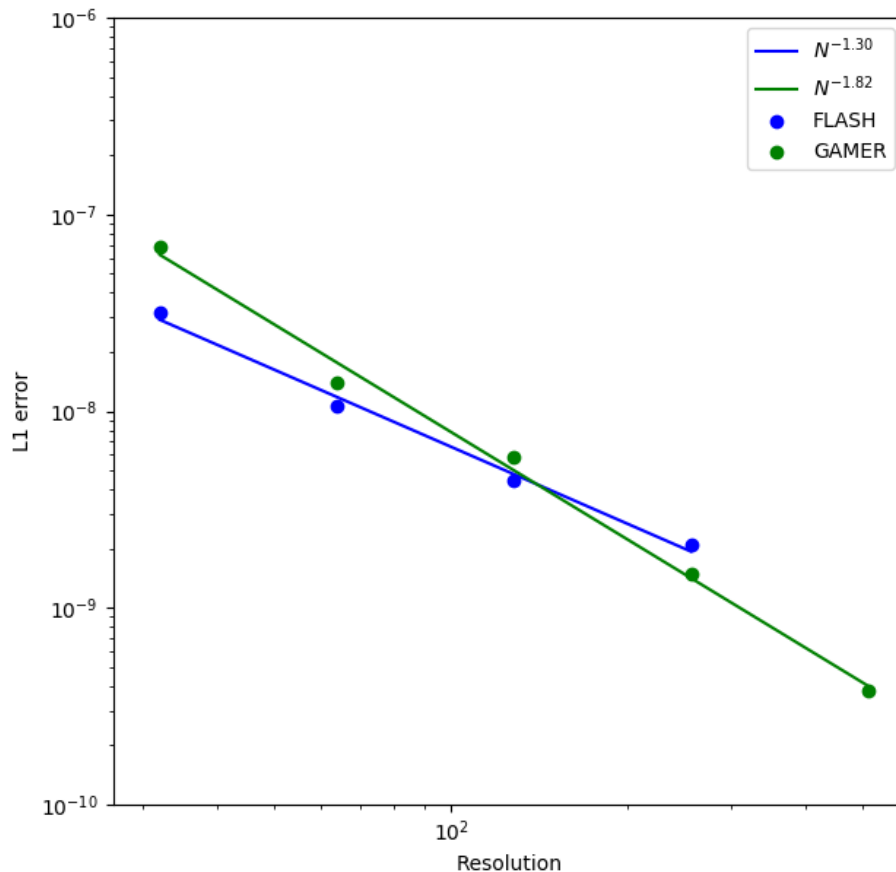
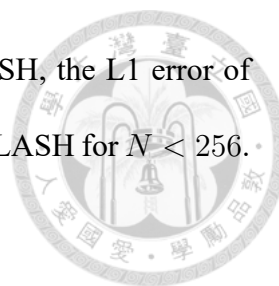


Figure 3.4: Sound wave test of the cosmic rays and the thermal gas. The figure shows the L1 error convergence. The L1 error of the Yang et al., 2012 algorithm is plotted as blue dots; the L1 error of GAMER is plotted as green dots; the solid blue line is the linear fitting of the Yang et al., 2012 algorithm. L1 error; the green solid line represents the linear fit of the GAMER L1 error.



Since the hydro solver is more diffusive in GAMER than FLASH, the L1 error of GAMER is greater than Yang et al., 2012 algorithm implemented in FLASH for $N < 256$.

3.1.2 Half Step Update

Continuing the previous sections, we explain why GAMER shows a better error scaling than the Yang et al., 2012 algorithm. Since the Yang et al., 2012 algorithm does not update the adiabatic work term in the half-step, so we expect the error convergence rate of GAMER to be better. Now, we remove the adiabatic work update at half-step by hard-coded, so the GAMER now has the same algorithm as the Yang et al., 2012 algorithm. As shown in figure 3.5, the L1 error of updated adiabatic work term in half-step is proportional to $N^{-1.82}$, and the L1 error of not updated the adiabatic work term in half-step is proportional to $N^{-1.50}$.

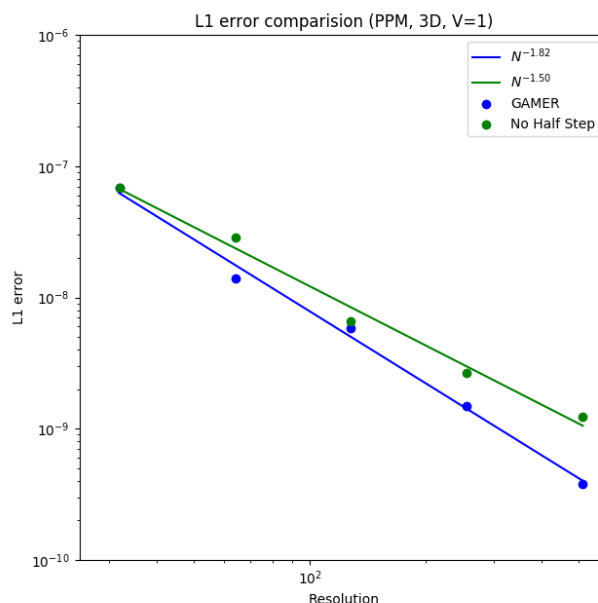


Figure 3.5: Sound wave test of the cosmic rays and thermal gas. The figure shows the L1 error convergence. The L1 error of GAMER without a half-step update is plotted as blue dots; the L1 error of GAMER with a half-step update is plotted as green dots; the solid blue line is the linear fitting of GAMER without a half-step update L1 error; the solid green line is the linear fitting GAMER with half-step update L1 error.



3.2 Shock Tube (without diffusion)

The shock-tube test is one of the standard tests in MHD code. The boundary condition is the Dirichlet boundary condition which is determined by the left and the right states. The resolution of the test is 128 along the shock propagation direction. The left state ($0 < x < 0.5$) and the right state ($0.5 \leq x < 1$) are initialized as the given table 3.1 [35] [30].

Parameter	Left	Right
ρ	1.0	0.2
\mathbf{v}	0.0	0.0
p_{th}	6.7×10^4	2.4×10^2
p_{cr}	1.3×10^5	2.4×10^2

Table 3.1: The initial condition of the shock tube test. From the top to the bottom, the parameters are density, velocity, gas pressure, and cosmic rays pressure.

As shown in the figure (3.6), the simulation result agrees with the analytical solution. Since the hydro solver is more diffusive in GAMER, the shock in GAMER is slightly more diffusive than that in Yang et al., 2012 algorithm. In general, the result from GAMER is also similar to the result from Yang et al., 2012 algorithm.

3.3 Diffusion

In this section, all the fluids except cosmic rays are fixed in the following tests, and we do not update the adiabatic work term. Hence, the only equation we are solving is

$$\frac{\partial e_{cr}}{\partial t} = \nabla \cdot (\boldsymbol{\kappa} \cdot \nabla e_{cr}) \quad (3.4)$$

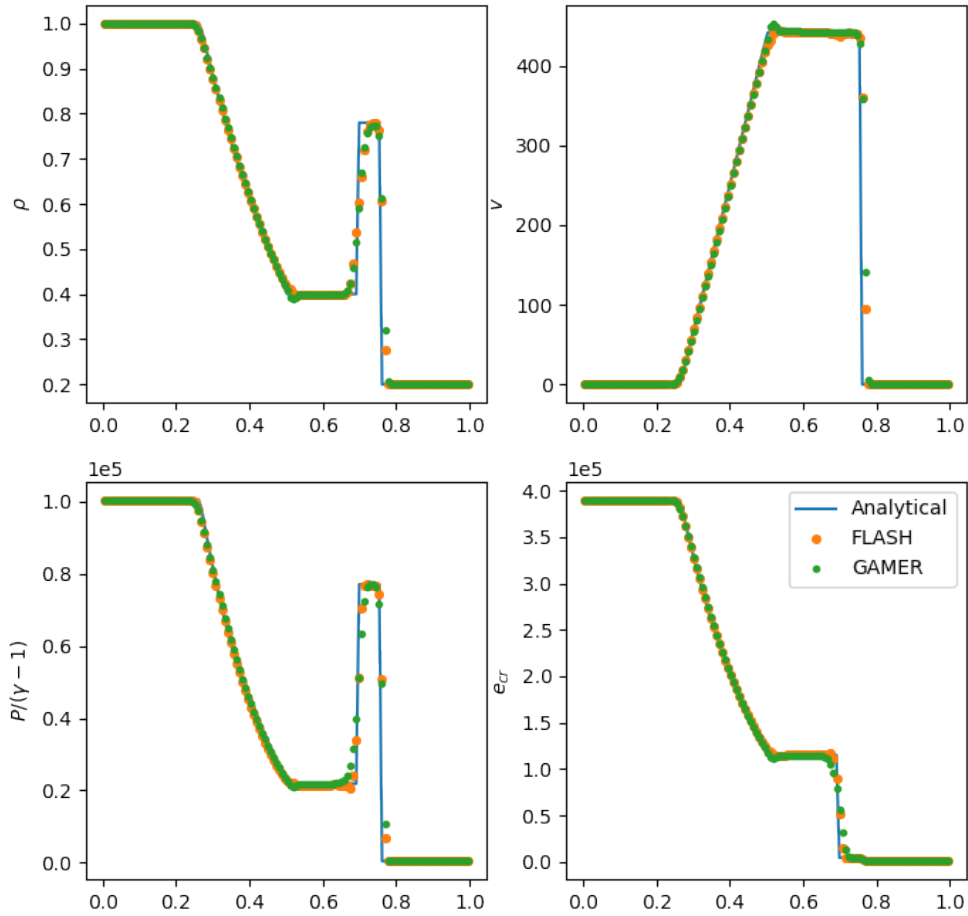


Figure 3.6: Shock tube test of the cosmic rays and the thermal gas. The top-left panel of the figure illustrates the density, the top-right panel displays the velocity, the bottom-left panel showcases the internal energy density of the gas, and the bottom-right panel exhibits the energy density of cosmic rays. The green dots show the GAMER simulation data; the orange dots show the Yang et al., 2012 algorithm simulation data; the blue solid lines represent the analytical solution.

which is a pure diffusion equation. In our implementation, the diffusion coefficient is separated into two parts, which are parallel diffusion coefficient κ_{\parallel} and perpendicular diffusion coefficient κ_{\perp} . The parallel and perpendicular directions are defined by the magnetic field locally. For the following test, the diffusion coefficients are both constants only.

3.3.1 Isotropic diffusion

We place a 3-D Gaussian distribution of cosmic rays energy density

$$e_{cr}(r) = 0.1e^{-Rr^2} + 0.1 \quad (3.5)$$

where $R^2 = 40$, and $r = \sqrt{x^2 + y^2 + z^2}$, and set a uniform magnetic field $B_x = 1.0 \times 10^{-10}$, $B_y = B_z = 0$, and the diffusion coefficients are set as $\kappa_{\parallel} = \kappa_{\perp} = 0.05$. The rest fluid variables are set as uniform at the background which are $\rho = 1.0$, $\mathbf{v} = 0$, $p_{th} = 100$. The analytical solution is given by (B.6).

The time evolution profile is shown in figure (3.7), the cosmic rays diffuse isotropically. As shown in figure (3.8), the L1 error is proportional to $N^{-1.79}$.

3.3.2 Anisotropic diffusion - Gaussian

The initial conditions are set to be the same as the previous subsection, but we change the parallel diffusion coefficient to $\kappa_{\parallel} = 0.05$ and perpendicular diffusion coefficient $\kappa_{\perp} = 0.0$, and the magnetic field to $B_x = B_y = 1.e - 10$, $B_z = 0$ uniformly, so the cosmic rays should diffuse along the x-y diagonal direction.

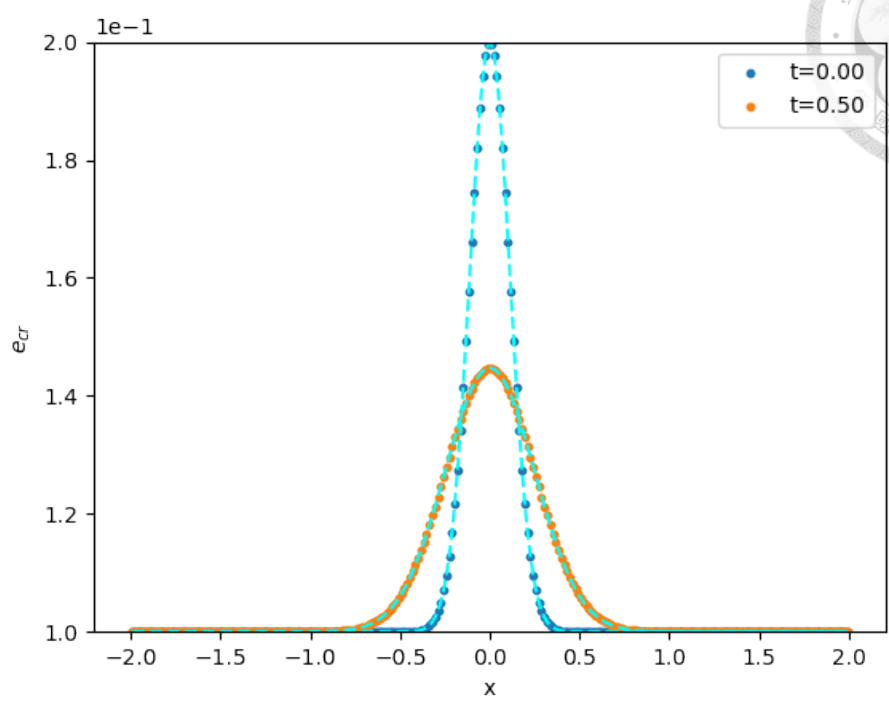


Figure 3.7: The figure shows the Gaussian distribution of cosmic rays energy density time evolution. The analytical solutions are marked as cyan dashed lines. The cosmic rays energy density is marked as blue and orange points at $t = 0$ and $t = 0.5$ respectively.

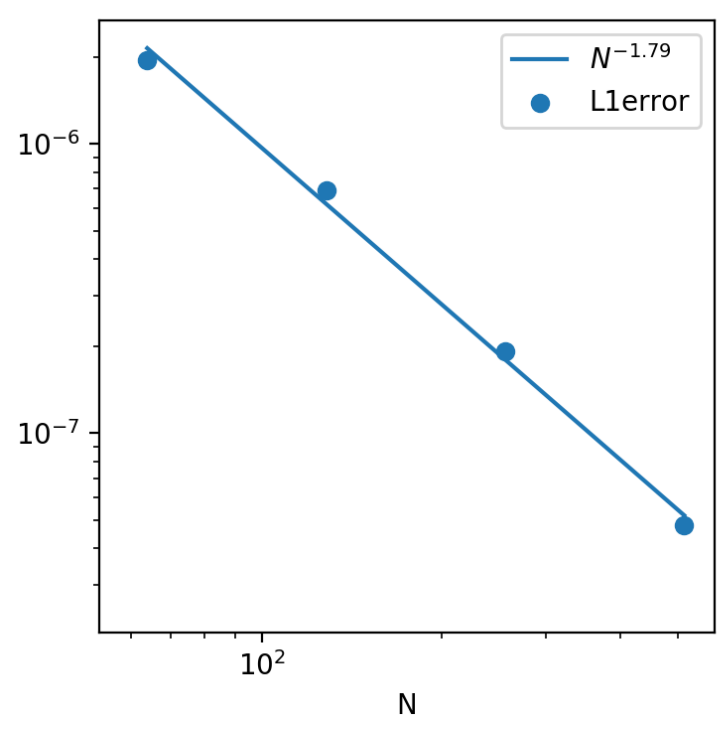


Figure 3.8: The L1 error of the isotropic diffusion test. The number of cells is set from 64^3 to 512^2 .

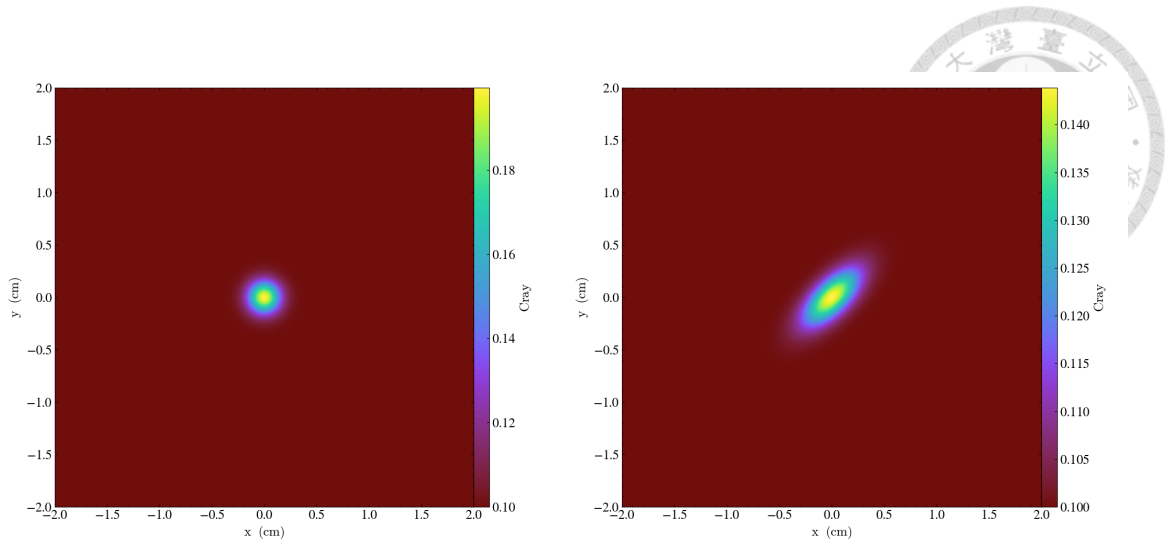


Figure 3.9: The x-y slice of the anisotropic diffusion test of the Gaussian distribution cosmic rays. The magnetic field is in the diagonal direction. The left panel is at $t=0$. The right panel is at $t=0.5$.

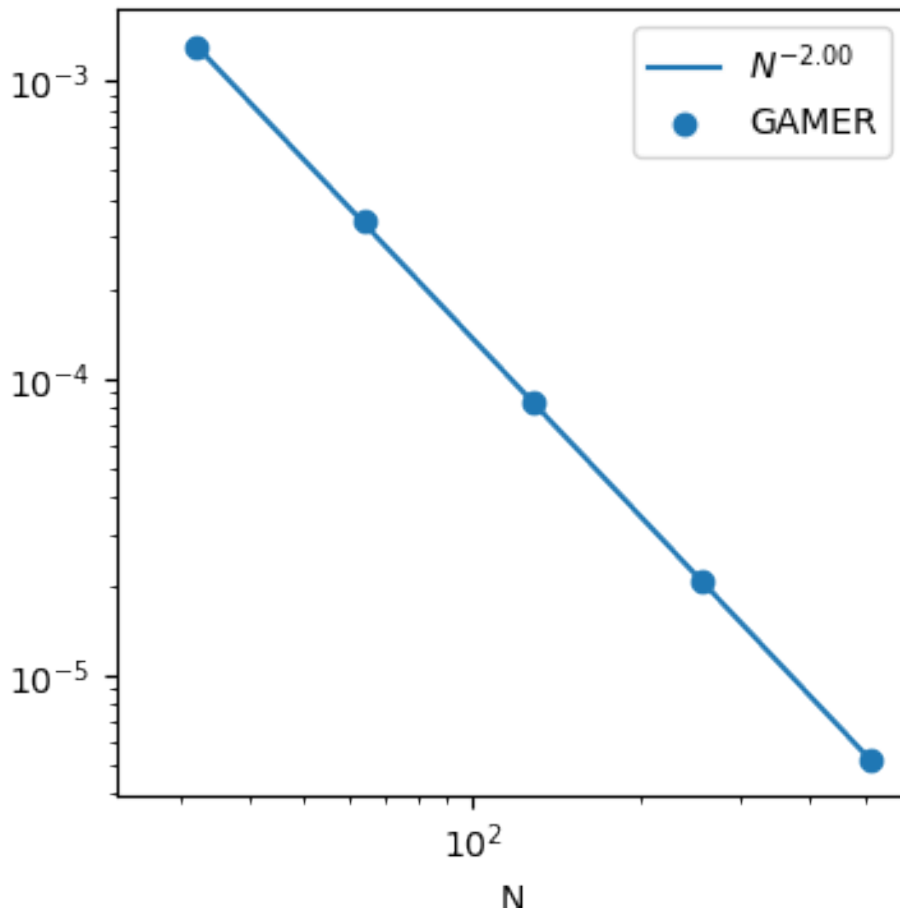
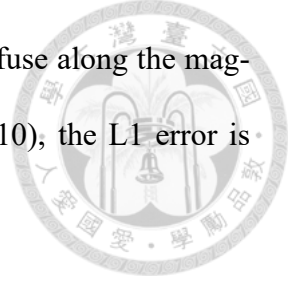


Figure 3.10: The L1 error of the two-dimensional anisotropic diffused cosmic rays.



The time evolution is shown in figure (3.9), the cosmic rays diffuse along the magnetic field which is the diagonal direction. As shown in figure (3.10), the L1 error is proportional to $N^{-2.00}$.

3.3.3 Anisotropic diffusion - Ring

There is one more challenging test problem for the anisotropic diffusion which is the ring test. The magnetic field is set as

$$\mathbf{B} = \left(-\frac{y}{r}, \frac{x}{r}, 0\right) \quad (3.6)$$

where $r = \sqrt{x^2 + y^2}$. The initial condition of cosmic rays density is set by

$$e_{cr}(x, y) = \begin{cases} 12 & , \text{if } 0.5 < r < 0.7, \text{ and } |\phi| \leq \frac{\pi}{12} \\ 10 & , \text{otherwise} \end{cases} \quad (3.7)$$

where $\phi = \arctan(\frac{y}{x})$, and other fixed fluid variables are set as $\rho = 1.0$, $\mathbf{v} = 0.0$, and $p_{th} = 100$.. The analytical solution in the short time which means the cosmic rays are not yet touch each other at $\phi = \pi$ is given by [20]

$$e_{cr}(x, y, t) = 10 + \text{Erfc} \left[\left(\phi - \frac{\pi}{12} \right) \frac{r}{D} \right] - \text{Erfc} \left[\left(\phi + \frac{\pi}{12} \right) \frac{r}{D} \right] \quad (3.8)$$

where $D = \sqrt{4t\kappa/3}$, and $\text{Erfc}(x)$ is the complementary error function (3.9).

$$\text{Erfc}(x) = \frac{2}{\sqrt{\pi}} \int_x^{\infty} e^{-t^2} dt \quad (3.9)$$

For the long-time solution, the energy is completely diffused along the azimuthal direction, so the cosmic rays remain constant inside the ring.

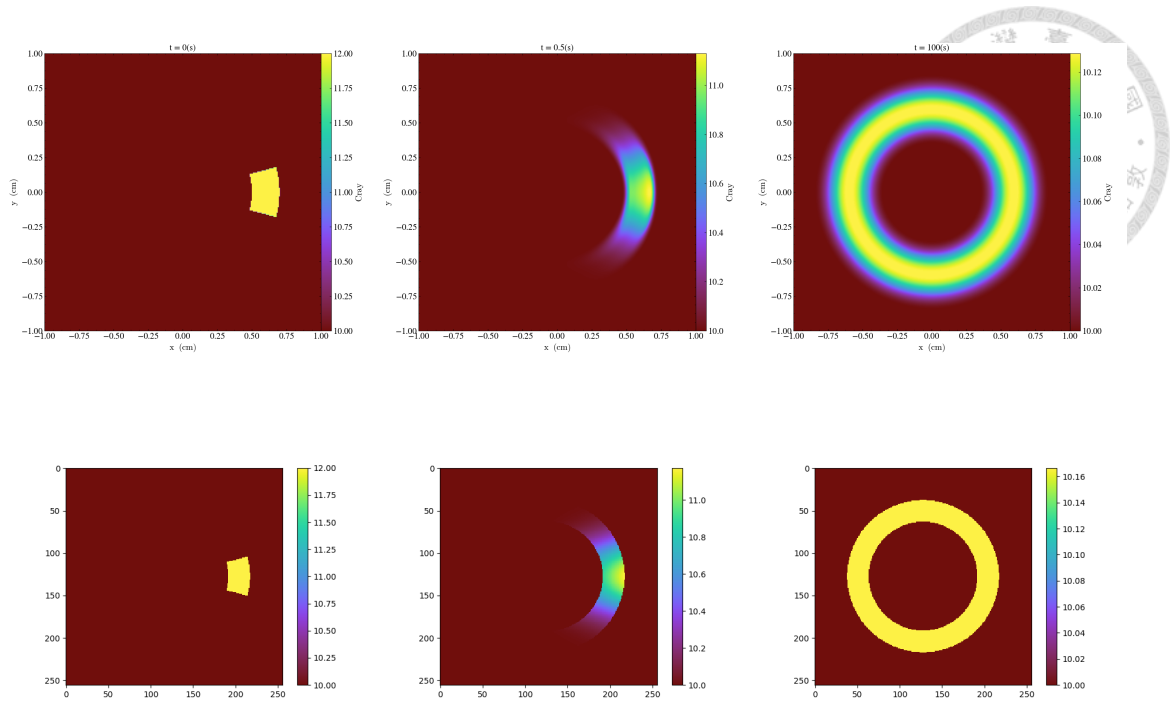


Figure 3.11: The ring test of the anisotropic diffusion. The top row figures are the simulation result, and the bottom row figures are the analytical solutions. The left column is $t = 0$. The middle column is $t = 0.1$. The right column is $t = 200$.

As you can see from the figure (3.11), the simulation agrees with the analytical solution. The reason for the blur at the boundary of the ring at the long time is that we used the square cell to run the simulation, so the ring boundary is not as sharp as the analytical solution. Hence, the L1 error of this test is less than second-order accuracy as shown in figure (3.12).

3.3.4 Anisotropic diffusion - Blast Wave

We place the high energy density cosmic rays in the center of the simulation box which has a uniform resolution of 128^3 . The cosmic rays energy density initial condition is set as

$$p_{cr} = \begin{cases} 100 & , \text{if } r < 0.02 \\ 0.1 & , \text{otherwise} \end{cases} \quad (3.10)$$

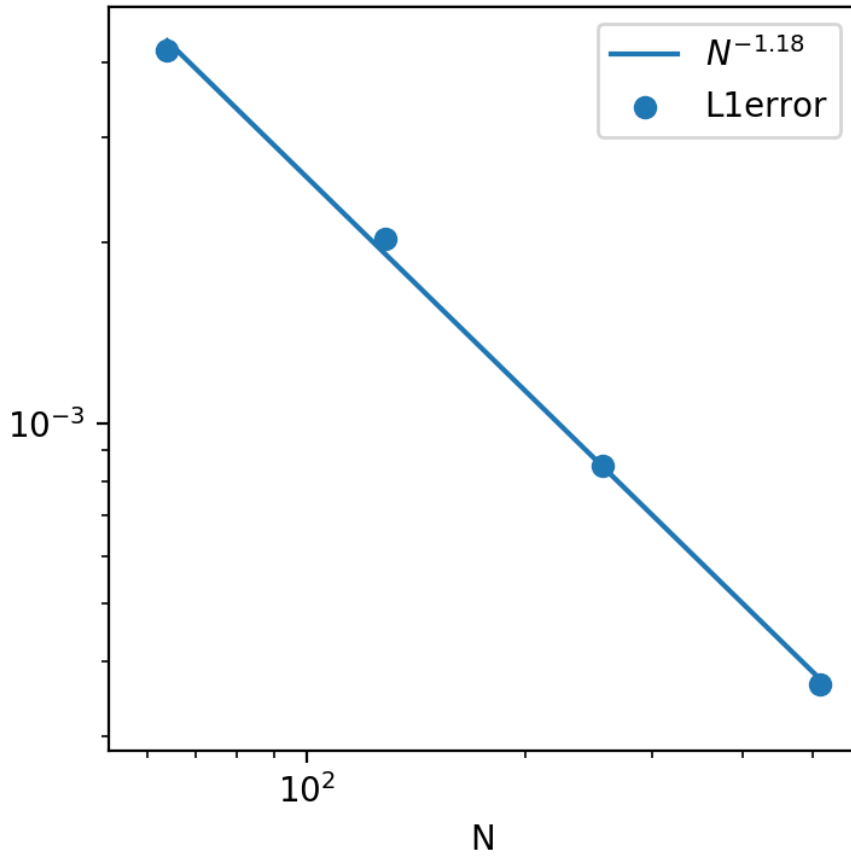


Figure 3.12: The figure shows the L1 error of the anisotropic diffuse cosmic rays ring test.

, the magnetic field is set as (3.11) where $B_0 = 5$, and $r_0 = 3.5 \times 10^9$, and other uniform initial conditions are set as $\rho = 1.0$, $\mathbf{v} = 0$, $p_{th} = 1.67$, the parallel diffusion coefficient $\kappa_{\parallel} = 0.05$, and the perpendicular one $\kappa_{\perp} = 0.0$ [36]. Our simulation domain is much smaller than r_0 , so the magnetic field is mainly along the z direction here.

$$\begin{aligned}
 B_x &= \frac{3B_0 x z r}{2r_0^3(1+r^3/r_0^3)^2} \\
 B_y &= \frac{3B_0 y z r}{2r_0^3(1+r^3/r_0^3)^2} \\
 B_z &= \frac{1}{r_0^3(1+r^3/r_0^3)^2} - \frac{3B_0(x^2+y^2)r}{2r_0^3(1+r^3/r_0^3)^2}
 \end{aligned} \tag{3.11}$$

As shown in figure (3.13), the cosmic rays only diffuse along the z direction since only the parallel diffusion coefficient is given. The gas is also pushed away by cosmic rays, so the inner low-density region also extends along the z direction.

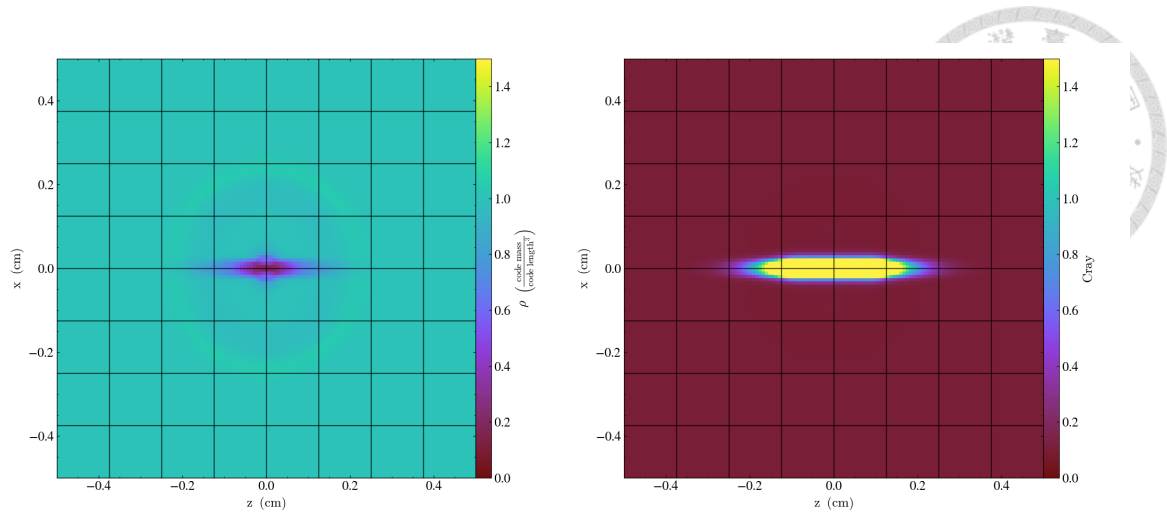


Figure 3.13: A x - z slice of the blast wave test of the anisotropic diffusion. The left panel presents the gas density, and the right panel illustrates the energy density of cosmic rays.

3.4 AMR

For the following tests, we use the Löhner error estimator as the criteria of refinement.

3.4.1 Blast wave

Here we use the same setup as 3.3.4 but with AMR refinement level up to level 3. As shown in figure (3.14), the simulation box is refined at the close center region only where the cosmic rays energy density has the larger gradient.

3.4.2 Shocktube

Here we use the same setup as section 3.2, but we change N of the uniform grid to be 1024 and the base resolution of 128 with AMR refinement level up to 3, so the maximum resolution is the same. As shown in figure (3.15), the region close to shock can be resolved clearly as uniform resolution, and also using fewer points to resolve the smooth region.

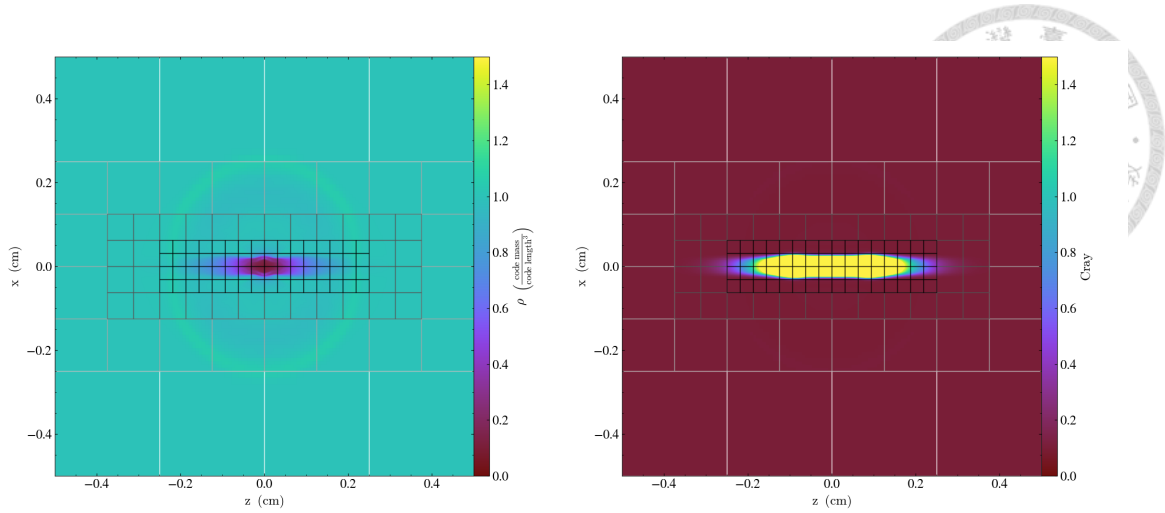


Figure 3.14: A x-z slice of blast wave test with anisotropic diffusion and AMR level up to 3. The left panel presents the gas density, and the right panel illustrates the energy density of cosmic rays.

3.5 Performance

We would like to know how much the performance drop of solving an extra cosmic rays evolution, and the scaling of parallel efficiency. We measure the computation time of one time-step in the simulation with double precision as the performance. We set N to be 512^3 , and the diffusion of cosmic rays is disabled. The CPU we used is AMD Threadripper 2950X, and the GPU we used is GeForce RTX 2080 SUPER.

Core #	1	2	4	8	16	16 with GPU
Pure Hydro	372	193	102	57	33	17
Speed up	100%	193%	364%	652%	1127%	2188%
With CR	376	195	103	59	34	18
Speed up	100%	192%	365%	637%	1105%	2088%

Table 3.2: The computation time of one time-step with double precision.

As shown in 3.2, the performance of solving an extra evolution of cosmic rays does not make a huge difference compared to the original one. Also, the scaling of the parallel efficiency is similar to the original hydro scaling.

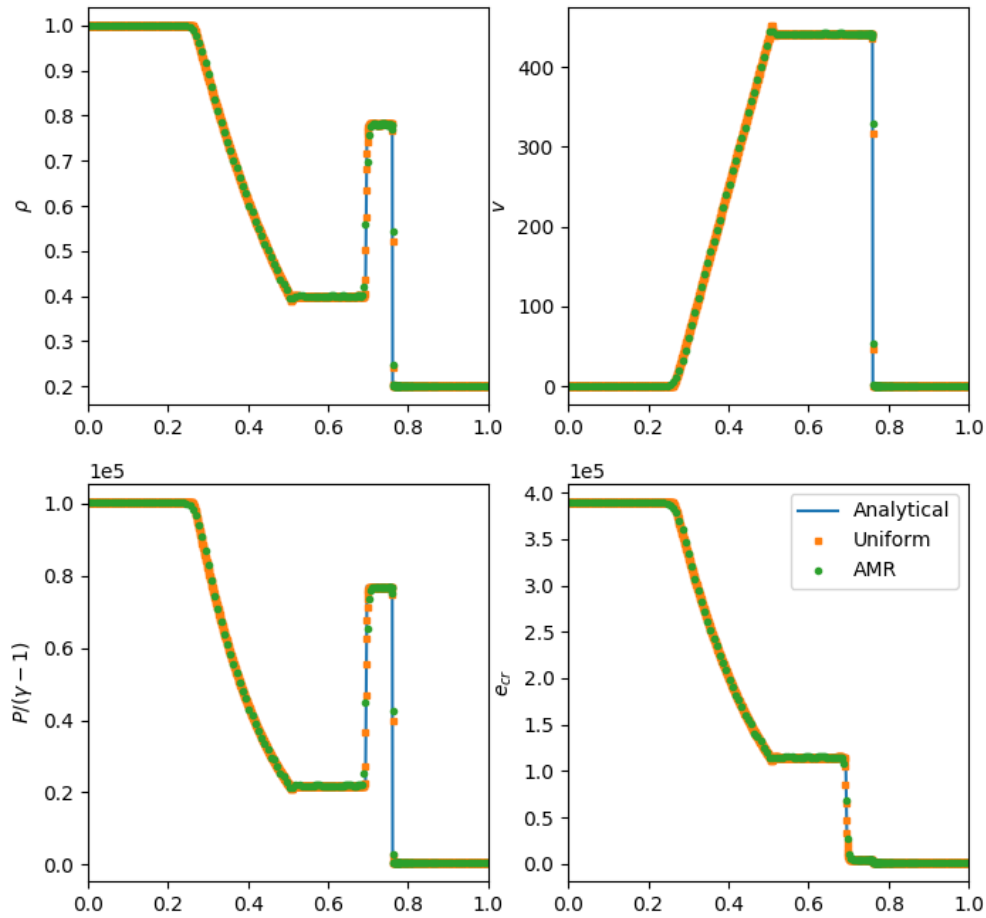


Figure 3.15: Shock tube test of cosmic rays and the thermal gas with and without AMR. The top-left panel of the figure illustrates the density, the top-right panel displays the velocity, the bottom-left panel showcases the internal energy density of the gas, and the bottom-right panel exhibits the energy density of cosmic rays. The green squares show the data with AMR; the orange dots represent the data without AMR; the blue solid lines represent the analytical solution of the shock tube.





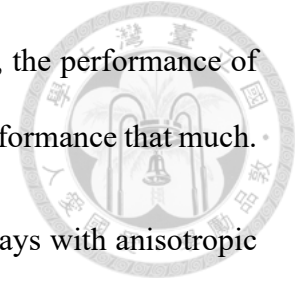
Chapter 4 Conclusions

We assume the collective speed of cosmic rays is the same as the surrounding thermal gas with single energy channel, and neglect the heating and the streaming effect. Based on the assumptions of cosmic rays, we have the MHD equations including the physics of cosmic rays. Using the MHM-RP time evolving algorithm and an extra half-step update of the cosmic rays adiabatic work, we have a better error convergence rate compared to Yang et al., 2012. algorithm.

To test the implementation of cosmic rays in GAMER, we use a series of tests to verify. First, we set a diagonal propagated sound wave and the error convergence rate is close to second order with and without the background velocity. Second, we set a shock-tube test to verify the non-linear effect of the cosmic rays, and the result agrees with the analytical solutions. Third, we set all the fluid to be fixed to test the diffusion implementation. We set a Gaussian distribution cosmic rays energy density with isotropic diffusion and also anisotropic diffusion, both of them give the second-order error convergence rate. Next, in an anisotropic ring test, we only have a first-order error convergence rate here since we used the Cartesian grid to evolve the cosmic rays. Fourth, We place the high energy density cosmic rays to evolve a cosmic rays driven blast wave, and we have a similar result compared to the Yang et al., 2012 algorithm. Fifth, we use the blast wave and the shock-tube test to verify the AMR function, both of them gives similar result and save

computational resources in the region we are not interested. Finally, the performance of solving an extra cosmic rays evolution does not affect the original performance that much.

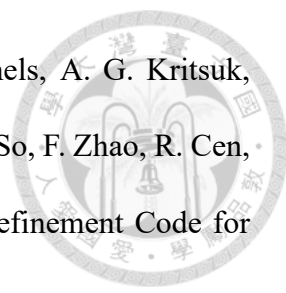
We have successfully implemented the single-channel cosmic rays with anisotropic diffusion, and our code also supports hybrid CPU/GPU parallelization. Furthermore, we would like to enhance our implementation by incorporating additional cosmic rays features, such as streaming, heating, and multi-channel cosmic rays.



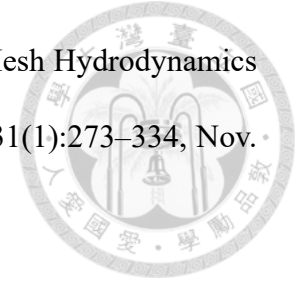


References

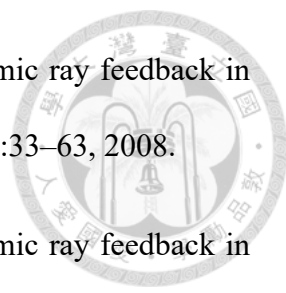
- [1] A. S. Almgren, V. E. Beckner, J. B. Bell, M. S. Day, L. H. Howell, C. C. Joggerst, M. J. Lijewski, A. Nonaka, M. Singer, and M. Zingale. CASTRO: A NEW COMPRESSIBLE ASTROPHYSICAL SOLVER. i. HYDRODYNAMICS AND SELF-GRAVITY. The Astrophysical Journal, 715(2):1221–1238, may 2010.
- [2] C. M. Booth, O. Agertz, A. V. Kravtsov, and N. Y. Gnedin. Simulations of disk galaxies with cosmic ray driven galactic winds. The Astrophysical Journal Letters, 777(1):L16, oct 2013.
- [3] C. M. Booth, O. Agertz, A. V. Kravtsov, and N. Y. Gnedin. Simulations of disk galaxies with cosmic ray driven galactic winds. The Astrophysical Journal Letters, 777(1):L16, oct 2013.
- [4] S. I. Braginskii. Transport Processes in a Plasma. Reviews of Plasma Physics, 1:205, Jan. 1965.
- [5] G. Brunetti and T. W. Jones. Cosmic Rays in Galaxy Clusters and Their Nonthermal Emission. International Journal of Modern Physics D, 23(4):1430007–98, Mar. 2014.
- [6] G. L. Bryan, M. L. Norman, B. W. O’Shea, T. Abel, J. H. Wise, M. J. Turk, D. R. Reynolds, D. C. Collins, P. Wang, S. W. Skillman, B. Smith, R. P. Harkness, J. Bor-

- 
- ner, J.-h. Kim, M. Kuhlen, H. Xu, N. Goldbaum, C. Hummels, A. G. Kritsuk, E. Tasker, S. Skory, C. M. Simpson, O. Hahn, J. S. Oishi, G. C. So, F. Zhao, R. Cen, Y. Li, and Enzo Collaboration. ENZO: An Adaptive Mesh Refinement Code for Astrophysics. , 211(2):19, Apr. 2014.
- [7] T. K. Chan, D. Kereš, P. F. Hopkins, E. Quataert, K.-Y. Su, C. C. Hayward, and C.-A. Faucher-Giguère. Cosmic ray feedback in the FIRE simulations: constraining cosmic ray propagation with GeV γ -ray emission. Monthly Notices of the Royal Astronomical Society, 488(3):3716–3744, 07 2019.
- [8] P. Colella. Multidimensional upwind methods for hyperbolic conservation laws. Journal of Computational Physics, 87(1):171–200, 1990.
- [9] P. Colella and P. R. Woodward. The piecewise parabolic method (ppm) for gas-dynamical simulations. Journal of Computational Physics, 54(1):174–201, 1984.
- [10] R. Courant, K. Friedrichs, and H. Lewy. Über die partiellen Differenzgleichungen der mathematischen Physik. Mathematische Annalen, 100:32–74, Jan. 1928.
- [11] Dashyan, Gohar and Dubois, Yohan. Cosmic ray feedback from supernovae in dwarf galaxies. A&A, 638:A123, 2020.
- [12] S. A. E. G. Falle. Self-similar jets. Monthly Notices of the Royal Astronomical Society, 250(3):581–596, 06 1991.
- [13] M. Farcy, J. Rosdahl, Y. Dubois, J. Blaizot, and S. Martin-Alvarez. Radiation-magnetohydrodynamics simulations of cosmic ray feedback in disc galaxies. Monthly Notices of the Royal Astronomical Society, 513(4):5000–5019, 04 2022.
- [14] B. Fryxell, K. Olson, P. Ricker, F. X. Timmes, M. Zingale, D. Q. Lamb, P. MacNeice,

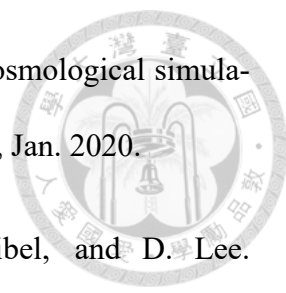
R. Rosner, J. W. Truran, and H. Tufo. FLASH: An Adaptive Mesh Hydrodynamics Code for Modeling Astrophysical Thermonuclear Flashes. , 131(1):273–334, Nov. 2000.



- [15] J. Fu, G. Kauffmann, M.-l. Huang, R. M. Yates, S. Moran, T. M. Heckman, R. Davé, Q. Guo, and B. M. B. Henriques. Star formation and metallicity gradients in semi-analytic models of disc galaxy formation. , 434(2):1531–1548, Sept. 2013.
- [16] X. Guo, L. Sironi, and R. Narayan. Non-thermal electron acceleration in low mach number collisionless shocks. ii. firehose-mediated fermi acceleration and its dependence on pre-shock conditions. The Astrophysical Journal, 797(1):47, nov 2014.
- [17] M. Hanasz, H. Lesch, T. Naab, A. Gawryszczak, K. Kowalik, and D. Wóltanski. Cosmic rays can drive strong outflows from gas-rich high-redshift disk galaxies. The Astrophysical Journal Letters, 777(2):L38, oct 2013.
- [18] P. F. Hopkins, T. K. Chan, S. Garrison-Kimmel, S. Ji, K.-Y. Su, C. B. Hummels, D. Kereš, E. Quataert, and C.-A. Faucher-Giguère. But what about...: cosmic rays, magnetic fields, conduction, and viscosity in galaxy formation. Monthly Notices of the Royal Astronomical Society, 492(3):3465–3498, 12 2019.
- [19] P. F. Hopkins, T. K. Chan, S. Ji, C. B. Hummels, D. Kereš, E. Quataert, and C.-A. Faucher-Giguère. Cosmic ray driven outflows to Mpc scales from L^* galaxies. Monthly Notices of the Royal Astronomical Society, 501(3):3640–3662, 11 2020.
- [20] Y.-F. Jiang and S. P. Oh. A new numerical scheme for cosmic-ray transport. The Astrophysical Journal, 854(1):5, feb 2018.
- [21] M. Jubelgas, V. Springel, T. Enßlin, and C. Pfrommer. Cosmic ray feedback in hydrodynamical simulations of galaxy formation. , 481(1):33–63, Apr. 2008.

- 
- [22] Jubelgas, M., Springel, V., Enßlin, T., and Pfrommer, C. Cosmic ray feedback in hydrodynamical simulations of galaxy formation. *A&A*, 481(1):33–63, 2008.
- [23] Jubelgas, M., Springel, V., Enßlin, T., and Pfrommer, C. Cosmic ray feedback in hydrodynamical simulations of galaxy formation. *A&A*, 481(1):33–63, 2008.
- [24] S. Li. A Simple Dual Implementation to Track Pressure Accurately. In N. V. Pogorelov, E. Audit, and G. P. Zank, editors, *Numerical Modeling of Space Plasma Flows*, volume 385 of *Astronomical Society of the Pacific Conference Series*, page 273, Apr. 2008.
- [25] R. Löhner, K. Morgan, J. Peraire, and M. Vahdati. Finite element flux-corrected transport (fem-fct) for the euler and navier–stokes equations. *International Journal for Numerical Methods in Fluids*, 7(10):1093–1109, 1987.
- [26] T. Miyoshi and K. Kusano. A multi-state HLL approximate Riemann solver for ideal magnetohydrodynamics. *Journal of Computational Physics*, 208(1):315–344, Sept. 2005.
- [27] F. R. Montero, S. Martin-Alvarez, A. Slyz, J. Devriendt, Y. Dubois, and D. Sijacki. The impact of cosmic rays on the interstellar medium and galactic outflows of milky way analogues, 2023.
- [28] R. Pakmor, C. Pfrommer, C. M. Simpson, and V. Springel. Galactic winds driven by isotropic and anisotropic cosmic-ray diffusion in disk galaxies. *The Astrophysical Journal Letters*, 824(2):L30, jun 2016.
- [29] N. Peschken, M. Hanasz, T. Naab, D. Wóltański, and A. Gawryszczak. The phase structure of cosmic ray driven outflows in stream fed disc galaxies. *Monthly Notices of the Royal Astronomical Society*, 522(4):5529–5545, 05 2023.

- 
- [30] C. Pfrommer, V. Springel, T. A. Enßlin, and M. Jubelgas. Detecting shock waves in cosmological smoothed particle hydrodynamics simulations. Monthly Notices of the Royal Astronomical Society, 367(1):113–131, 03 2006.
- [31] Y. Rasera and B. Chandran. Numerical simulations of buoyancy instabilities in galaxy cluster plasmas with cosmic rays and anisotropic thermal conduction. The Astrophysical Journal, 685(1):105–117, Sep 2008.
- [32] R. J. Reynolds, L. M. Haffner, and S. L. Tufte. Evidence for an additional heat source in the warm ionized medium of galaxies. The Astrophysical Journal, 525(1):L21, sep 1999.
- [33] H.-Y. Schive, Y.-C. Tsai, and T. Chiueh. Gamer: A graphic processing unit accelerated adaptive-mesh-refinement code for astrophysics. The Astrophysical Journal Supplement Series, 186(2):457–484, feb 2010.
- [34] H.-Y. Schive, J. A. ZuHone, N. J. Goldbaum, M. J. Turk, M. Gaspari, and C.-Y. Cheng. gamer-2: a gpu-accelerated adaptive mesh refinement code – accuracy, performance, and scalability. Monthly Notices of the Royal Astronomical Society, 481(4):4815–4840, Sep 2018.
- [35] G. A. Sod. A survey of several finite difference methods for systems of nonlinear hyperbolic conservation laws. Journal of Computational Physics, 27(1):1–31, 1978.
- [36] Y. Suwa, T. Takiwaki, K. Kotake, and K. Sato. Magnetorotational collapse of population III stars. Publications of the Astronomical Society of Japan, 59(4):771–785, aug 2007.
- [37] R. Teyssier. Cosmological hydrodynamics with adaptive mesh refinement. A new high resolution code called RAMSES. , 385:337–364, Apr. 2002.

- 
- [38] M. Vogelsberger, F. Marinacci, P. Torrey, and E. Puchwein. Cosmological simulations of galaxy formation. Nature Reviews Physics, 2(1):42–66, Jan. 2020.
- [39] H.-Y. K. Yang, M. Ruszkowski, P. M. Ricker, E. Zweibel, and D. Lee. THE FERMI BUBBLES: SUPERSONIC ACTIVE GALACTIC NUCLEUS JETS WITH ANISOTROPIC COSMIC-RAY DIFFUSION. The Astrophysical Journal, 761(2):185, dec 2012.
- [40] U.-H. Zhang, H.-Y. Schive, and T. Chiueh. Magnetohydrodynamics with gamer. The Astrophysical Journal Supplement Series, 236(2):50, jun 2018.
- [41] J. G. Zheng, B. C. Khoo, and Z. M. Hu. Simulation of wave-flow-cavitation interaction using a compressible homogenous flow method. Communications in Computational Physics, 14(2):328–354, 2013.



Appendix A — GAMER Limiter

In this appendix, we will discuss how the limiter affects the order of accuracy. Here, we used three types of limiters, Generalized-MINMOD (limiter 2), Van Leer Generalized-MINMOD (limiter 4), and CENTRAL (limiter 6) to demonstrate.

We use the sound wave test in section (3.1) to test our limiter performance. For the one-dimensional traveling wave, the CENTRAL limiter has a better error convergence rate. And, we also have the same result for the three-dimensional traveling wave. The Van Leer Generalized-MINMOD has a better performance when there is a background velocity of the traveling wave.

Concluding the figure A.1-A.4, we can say that the CENTRAL limiter is better than the other limiters in general.

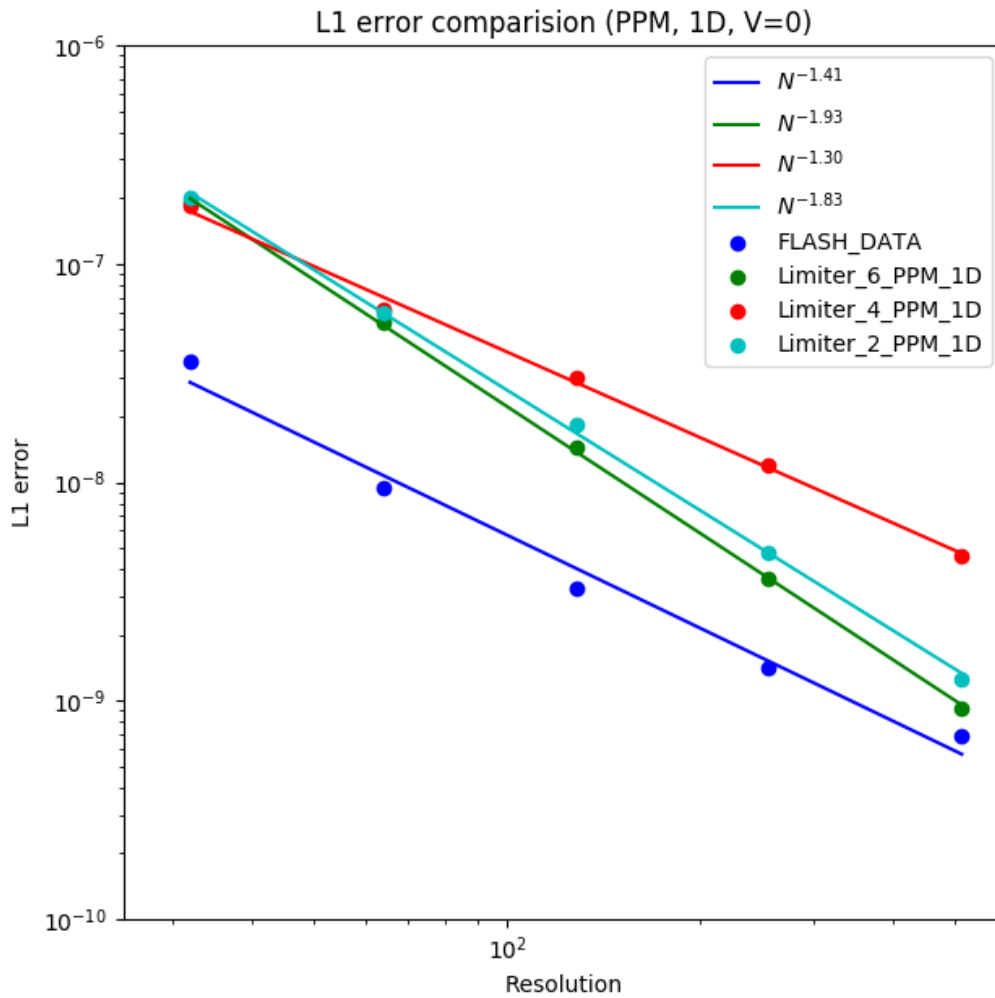


Figure A.1: The L1 error of the one-dimensional linear wave sound wave test without background velocity is shown in the figure. The L1 errors are represented by colored dots: blue for FLASH, green for GAMER limiter 6, red for GAMER limiter 4, and cyan for GAMER limiter 2. The solid lines indicate linear fittings for each L1 error.

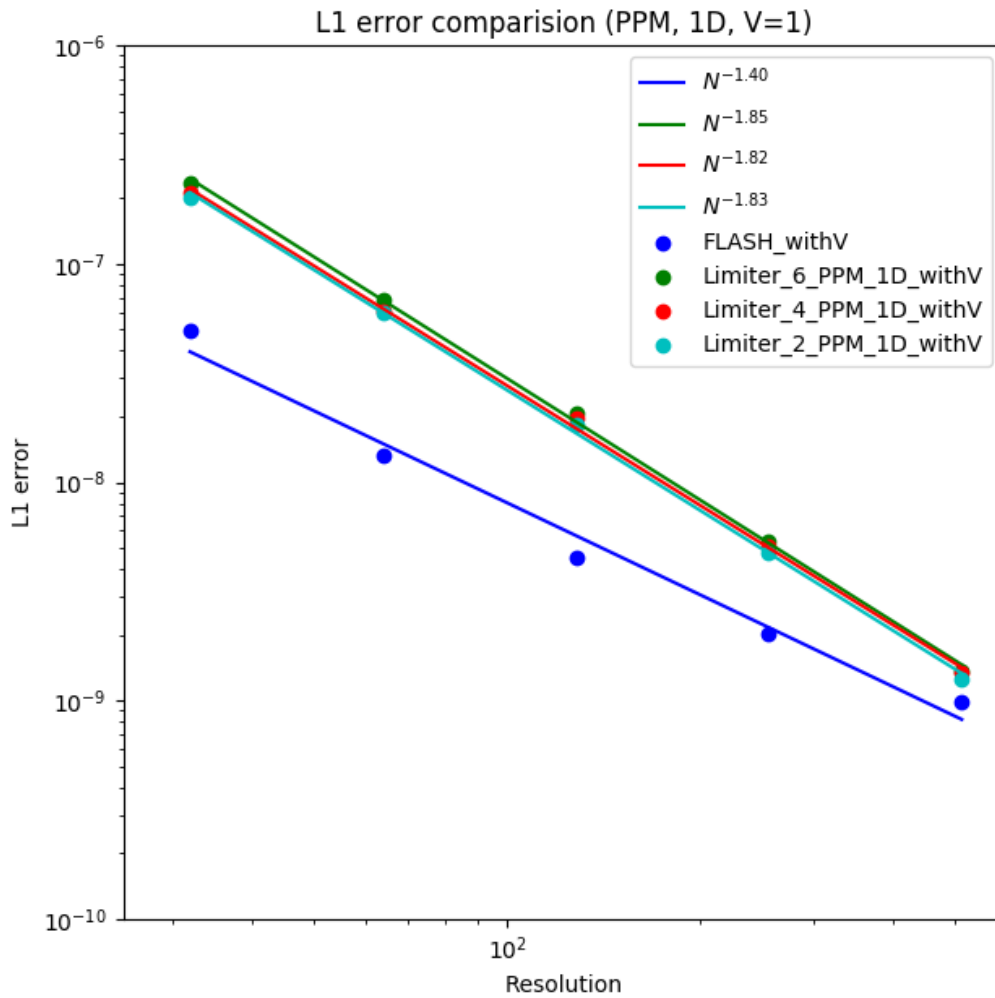


Figure A.2: The L1 error of the one-dimensional linear wave sound wave test with background velocity is shown in the figure. The L1 errors are represented by colored dots: blue for FLASH, green for GAMER limiter 6, red for GAMER limiter 4, and cyan for GAMER limiter 2. The solid lines indicate linear fittings for each L1 error.

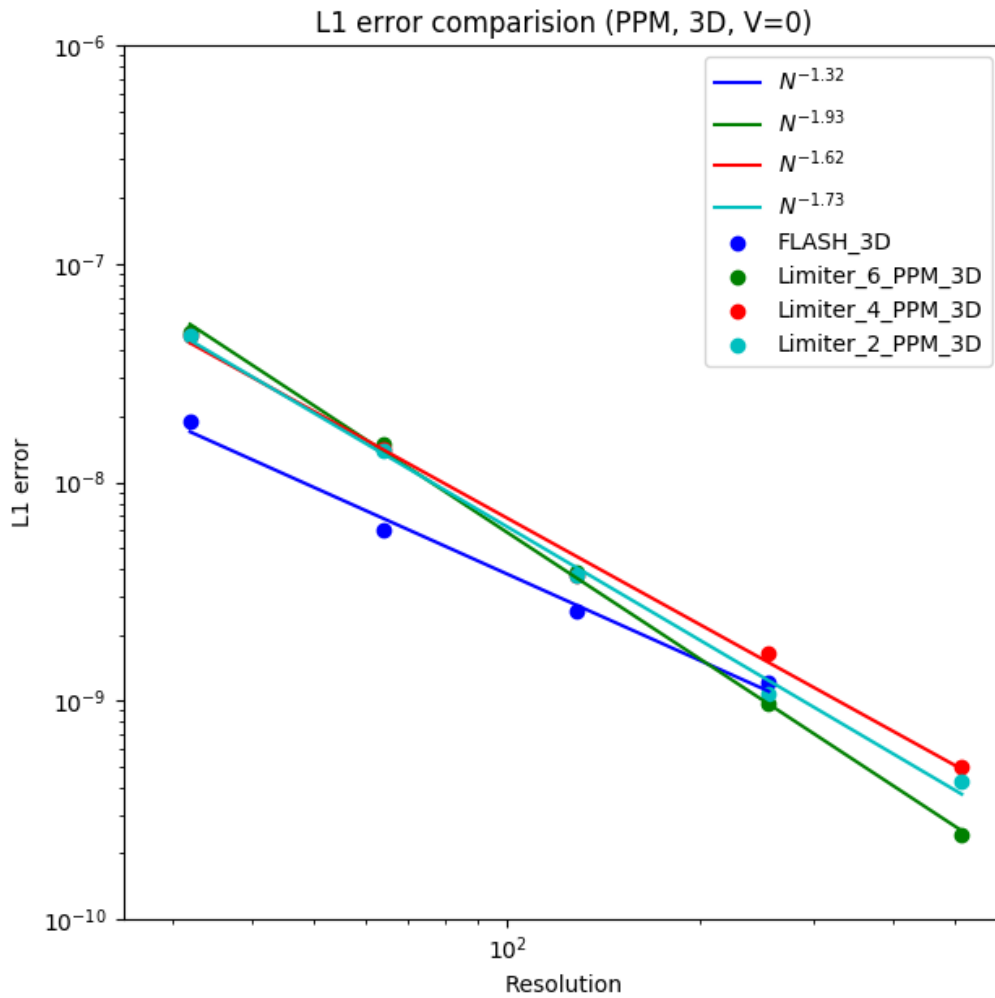


Figure A.3: The L1 error of the three-dimensional linear wave sound wave test without background velocity is shown in the figure. The L1 errors are represented by colored dots: blue for FLASH, green for GAMER limiter 6, red for GAMER limiter 4, and cyan for GAMER limiter 2. The solid lines indicate linear fittings for each L1 error.

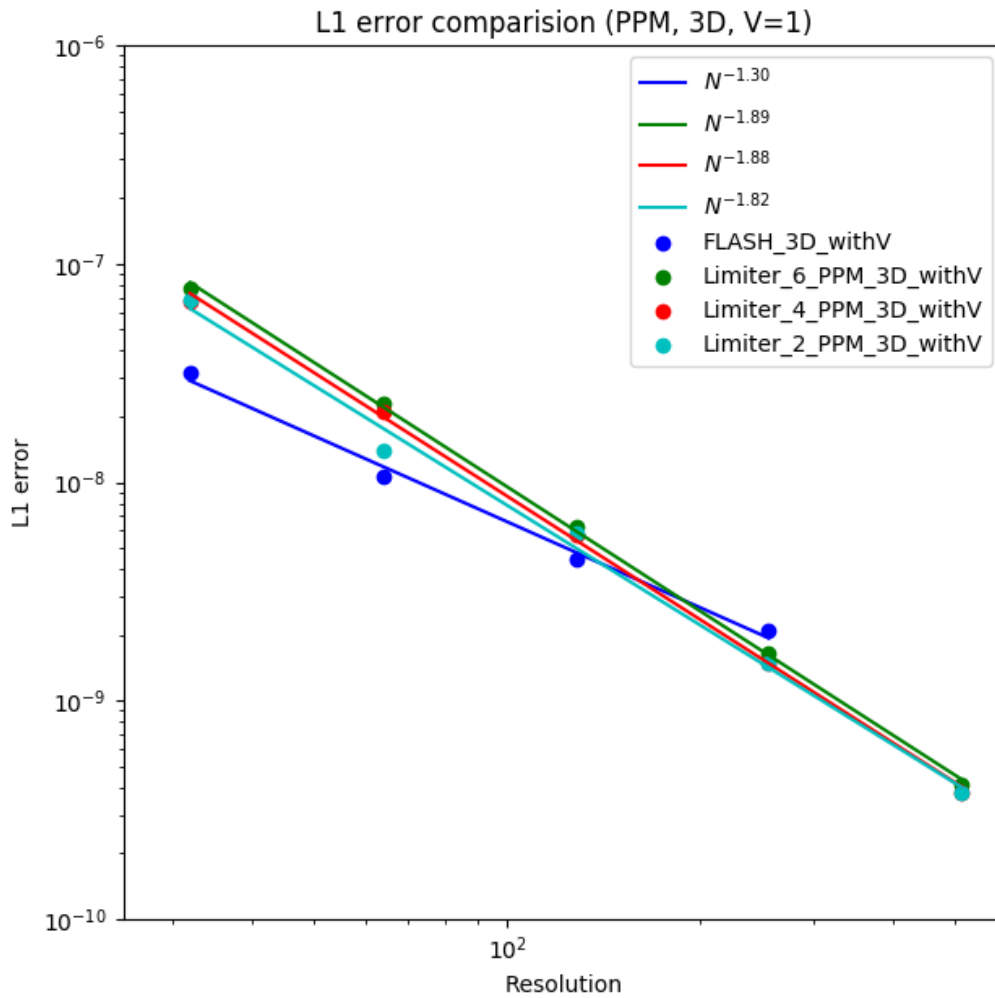


Figure A.4: The L1 error of the three-dimensional linear wave sound wave test with background velocity is shown in the figure. The L1 errors are represented by colored dots: blue for FLASH, green for GAMER limiter 6, red for GAMER limiter 4, and cyan for GAMER limiter 2. The solid lines indicate linear fittings for each L1 error.





Appendix B — Analytical Solution of CR Diffusion Equation

In this appendix, we will get the analytical solution of the cosmic rays diffusion. We will first get the one-dimensional diffusion solution, then we will extend it to the three-dimensional solution.

B.1 1-D solution

The one-dimensional diffusion equation of cosmic rays is shown as (B.1), where the $E(x, t)$ is the cosmic rays energy density as a function of space and time, and k is the diffusion coefficient along x direction.

$$\frac{\partial E(x, t)}{\partial t} = k \frac{\partial^2 E(x, t)}{\partial x^2} \quad (\text{B.1})$$

Here, we define a useful function $g(t) = 1 + 4Rkt$ for the calculation, where R is an arbitrary constant.

The analytical solution given by (B.2) where $B.G.$ is the background value of cosmic rays energy density.



$$\begin{aligned}
 E_{ana}(x, t) &= E_0 \frac{1}{\sqrt{1 + 4Rkt}} \exp \left[\frac{-Rx^2}{1 + 4Rkt} \right] + B.G. \\
 &= E_0 g^{-1/2} \exp \left[-Rx^2 g^{-1} \right] + B.G.
 \end{aligned} \tag{B.2}$$

Next, we verify if the given analytical solution is valid for (B.1). We now calculate the time derivative (B.3) and the second derivative of the space (B.4) of the analytical solution (B.2).

$$\begin{aligned}
 \frac{\partial E_{ana}}{\partial t} &= -\frac{1}{2} g^{-1} (4Rk) E_{ana} + Rx^2 g^{-2} (4Rk) E_{ana} \\
 &= k \left[-2Rg^{-1} + 4R^2 x^2 g^{-2} \right] E_{ana}
 \end{aligned} \tag{B.3}$$

$$\begin{aligned}
 \frac{\partial^2 E_{ana}}{\partial x^2} &= -R2g^{-1} E_{ana} + R2xg^{-1} R2xg^{-1} E_{ana} \\
 &= \left[-2Rg^{-1} + 4R^2 x^2 g^{-2} \right] E_{ana}
 \end{aligned} \tag{B.4}$$

Combining (B.3) and (B.4), we have the analytical solution which satisfied the (B.1).

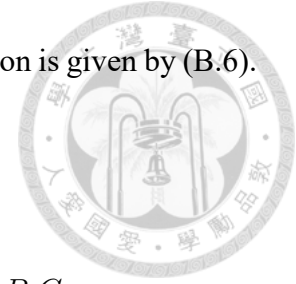
B.2 3-D solution

For the three-dimensional diffusion, the diffusion equation is shown as (B.5).

$$\frac{\partial E(r, t)}{\partial t} = \mathbf{k} \nabla^2 E(r, t) \tag{B.5}$$

And, we define the useful function as now rewrite as $g_i(t) = 1 + 4R_i k_i t$, where i stands for the x , y , and z , directions.

The analytical solution of the three-dimensional diffusion equation is given by (B.6).



$$\begin{aligned}
 E_{ana}(r, t) &= E_0 \prod_{i=1}^3 \frac{1}{\sqrt{1 + 4R_i k_i t}} \exp \left[\frac{-R_i x_i^2}{1 + 4R_i k_i t} \right] + B.G. \\
 &= E_0 \prod_{i=1}^3 g_i^{-1/2} \exp [-R_i x_i^2 g_i^{-1}] + B.G.
 \end{aligned} \tag{B.6}$$

Next, we verify the solution same as the 1D diffusion case.

$$\begin{aligned}
 \frac{\partial E_{ana}}{\partial t} &= \sum_{i=1}^3 \left[-\frac{1}{2} g_i^{-1} (4R_i k_i) E_{ana} + R_i x_i^2 g_i^{-2} (4R_i k_i) E_{ana} \right] \\
 &= \sum_{i=1}^3 k_i [-2R_i g_i^{-1} + 4R_i^2 x_i^2 g_i^{-2}] E_{ana}
 \end{aligned} \tag{B.7}$$

$$\begin{aligned}
 \frac{\partial^2 E_{ana}(x, t)}{\partial x^2} &= \sum_{i=1}^3 [-R_i 2g_i^{-1} E_{ana} + R_i 2x_i g_i^{-1} R_i 2x_i g_i^{-1} E_{ana}] \\
 &= \sum_{i=1}^3 [-2R_i g_i^{-1} + 4R_i^2 x_i^2 g_i^{-2}] E_{ana}
 \end{aligned} \tag{B.8}$$

Combining (B.7) and (B.8), we have the analytical solution which satisfied the (B.5).